On-Chip Dynamic Mode Atomic Force Microscopy: A Silicon-on-Insulator MEMS Approach

Michael G. Ruppert, *Student Member, IEEE*, Anthony G. Fowler, *Member, IEEE*, Mohammad Maroufi, *Member, IEEE*, and S. O. Reza Moheimani, *Fellow, IEEE*

Abstract— The atomic force microscope (AFM) is an invaluable scientific tool; however, its conventional implementation as a relatively costly macroscale system is a barrier to its more widespread use. A microelectromechanical systems (MEMS) approach to AFM design has the potential to significantly reduce the cost and complexity of the AFM, expanding its utility beyond current applications. This paper presents an on-chip AFM based on a silicon-on-insulator MEMS fabrication process. The device features integrated xy electrostatic actuators and electrothermal sensors as well as an AlN piezoelectric layer for out-of-plane actuation and integrated deflection sensing of a microcantilever. The three-degree-of-freedom design allows the probe scanner to obtain topographic tapping-mode AFM images with an imaging range of up to 8μm × 8μm in closed loop.   [2016-0211]

Index Terms— Atomic force microscope, piezoelectric self-sensing, electrothermal sensing, electrostatic actuation, microelectromechanical systems (MEMS).

I. INTRODUCTION

FOR several decades, the atomic force microscope (AFM) has remained one of the primary instruments used for nanoscale object and material analysis in both research and industrial applications. At the heart of the AFM is a microcantilever with a sharp probe tip, which is scanned over the surface of a sample. By mapping the intermolecular forces that exist between the probe tip and the surface of the sample, the instrument is able to obtain the sample's topography and material properties with nanometer-scale resolution.

Since its introduction in the late 1980s [1], the AFM has generally been implemented as a macroscale system, with the instrument itself being many orders of magnitude larger than the size of the scan window. Conventionally, the in-plane scanning of the microcantilever is performed using piezoelectric tube scanners or flexure-guided nanopositioners, while the deflection of the microcantilever is measured using a laser and a position sensitive detector [2], [3]. While commercial

AFMs are often able to perform high-speed scanning with sub-nanometer resolution, their high cost of acquisition and the relative size of the hardware setup generally restricts their use to specialized laboratory-based applications.

More recently, microelecromechanical systems (MEMS)-based devices have emerged as a means of generating mechanical displacements with nanoscale precision in a much smaller form factor than that of conventional macroscale nanopositioners [4]–[6]. In addition, a MEMS implementation provides several other significant advantages, including much lower costs of fabrication, batch manufacturability, and potentially increased operating bandwidths [7], [8]. Given these potential benefits, we have previously explored the use of MEMS nanopositioners for AFM through the demonstration of silicon-on-insulator (SOI)-based devices as an AFM's scanning stage [9]–[12]. In [13], an in-plane MEMS nanopositioner with two degrees of freedom (DOF) was presented, which features electrostatic actuators and electrothermal sensors. The first resonance mode of the device along each axis is located at approximately 850 Hz, which enabled imaging in closed loop using a raster scan method with a maximum frequency of 100 Hz. However, the relatively low bandwidth of the device limits the maximum achievable imaging frequency. As such, a high-bandwidth 2-DOF MEMS nanopositioner was presented in [14] with more than 4.4 kHz bandwidth along each axis. AFM imaging of the device was performed using the raster scan method at 800 Hz in a window size of 8μm × 8μm. Non-raster trajectories such as Lissajous and spiral methods were also implemented for a novel MEMS nanopositioner in [10] and [15] respectively to achieve fast in-plane scans. Using these methods, much higher scan frequencies of 1000 Hz for the Lissajous method and 1430 Hz for spiral scanning were demonstrated.

Having successfully miniaturized one of the primary subsystems of the AFM, the next logical step is the development of a complete MEMS-based AFM. It is possible that the significant cost and portability improvements that may be achieved with the introduction of such a device may allow the AFM to move beyond its current role as a specialized scientific instrument.

In the literature, a single-chip AFM has been demonstrated that uses a CMOS-MEMS fabrication process [16], [17]. While the device has undergone a number of design iterations, it maintains the use of lateral and vertical electrothermal actuators to position a cantilever. The device is designed to operate in tapping mode, with the amplitude of the resonantly excited cantilever's oscillation being measured through the use
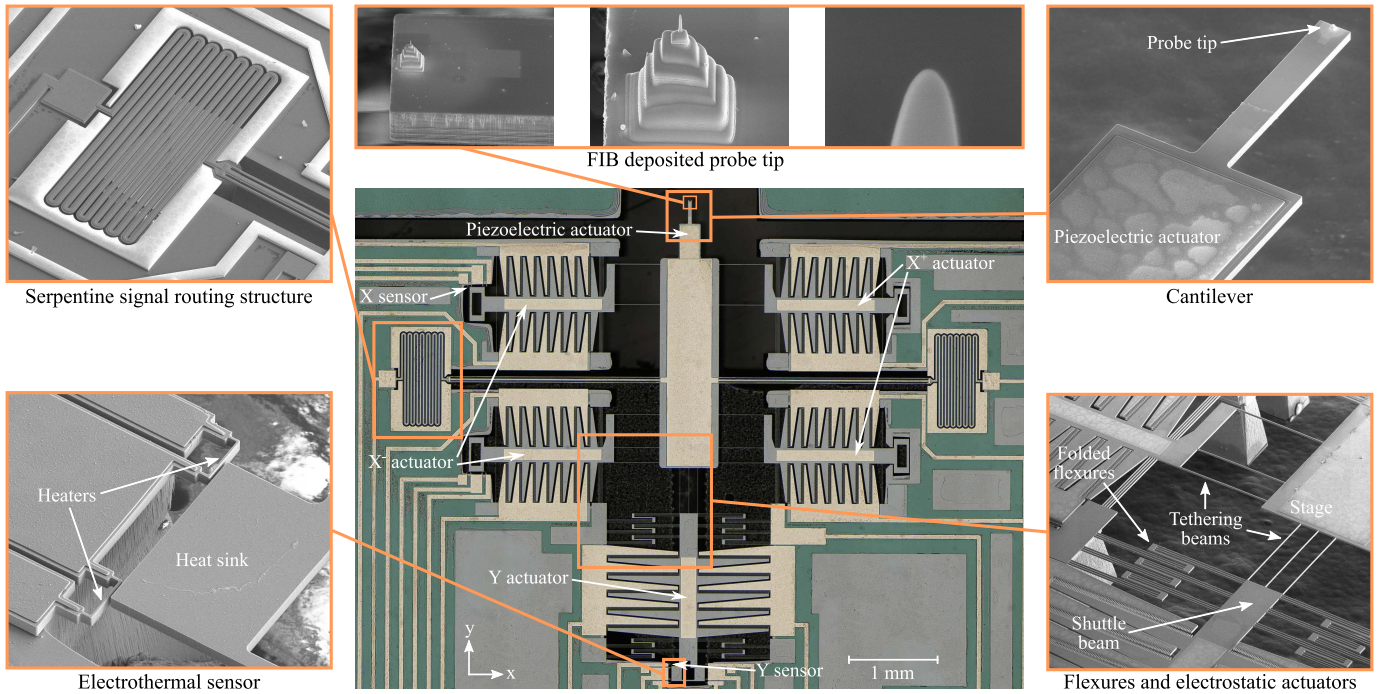
Fig. 1. The fabricated MEMS probe scanner, with close-up SEM images highlighting major components of the device. A serpentine structure for signal routing and an electrothermal sensor are shown in top-left and bottom-left close-up views, respectively. The close-up view in the top-right shows the cantilever and piezoelectric actuators. The bottom-right image shows the tethering and shuttle beams for the x and y axes, folded flexures along the y axis, and electrostatic actuators. The top close-up images show the FIB deposited tip on the cantilever for AFM imaging.

of piezoresistive sensing. The authors have successfully used the device to obtain topographical images of various samples, demonstrating the feasibility of a microfabricated AFM. However, the use of electrothermal actuation mechanisms potentially places a number of limitations on the performance of the device. Specifically, the operating bandwidth of electrothermal actuators is limited by their thermal mass and their rate of heat dissipation, therefore restricting the ultimate scan rate achievable by the AFM [18], [19]. In addition, electrothermal actuators use significantly more electrical power than other forms of MEMS actuators [20]. While power consumption may not be a major consideration for a standalone device, it may become an issue if attempts are made to increase the effective scan throughput by implementing multiple devices within an array.

Integrated cantilever actuation and sensing are paramount as the traditionally employed piezo stack actuator at the base of the cantilever and the optical beam deflection (OBD) method [21] are not compatible with the idea of a single-chip AFM. Furthermore, some of the integrated actuation methods found in the literature such as magnetic [22], photothermal [23], or ultrasonic [24] still require external equipment. As such, resistive thermal actuation [25] or via a piezoelectric layer [26] and integrated sensing methodologies such as capacitive [27], piezoresistive [28], and piezoelectric [29] sensing are fully compatible with an on-chip solution. Among these methods, piezoelectric transduction seems to be the only one capable of simultaneously serving as an actuator and a sensor even with a single active layer [30] which was therefore chosen for this work.

In [31], we introduced a microfabricated probe scanner, which demonstrated a novel SOI-MEMS approach to

designing an on-chip AFM. The device used electrostatic comb-finger actuators to laterally position a stage containing an integrated silicon cantilever. Using a dedicated piezoelectric actuator, the cantilever was driven at its out-of-plane vibrational mode at 62 kHz, however no AFM images were able to be obtained with the device as it did not possess a probe tip.

This paper presents a redesigned MEMS probe scanner that is again fabricated using a SOI-MEMS fabrication process. The device features a central stage that is positioned along the x and y axes using electrostatic actuators, with integrated electrothermal displacement sensors being implemented to facilitate closed-loop position control of the stage. A silicon microcantilever designed for tapping-mode AFM is fabricated at one end of the stage, and is actuated in the out-of-plane direction using a piezoelectric transducer made from a thin layer of aluminum nitride (AlN). Using a high-side charge sensing implementation motivated by previous work [32], the same piezoelectric transducer is also used to simultaneously measure the deflection of the cantilever. Following the addition of a probe tip to the end of the cantilever, the probe scanner is successfully used to perform AFM scans of features on a calibration grating.

II. PROBE SCANNER DESIGN AND FABRICATION

A. Mechanical Design

A scanning electron microscope (SEM) image of the MEMS probe scanner is shown in Fig. 1. The probe scanner is implemented using the standard SOI-based PiezoMUMPs fabrication process provided by MEMSCAP [33]. The thickness of the device layer, from which the entire structure is obtained, is 10 μm.
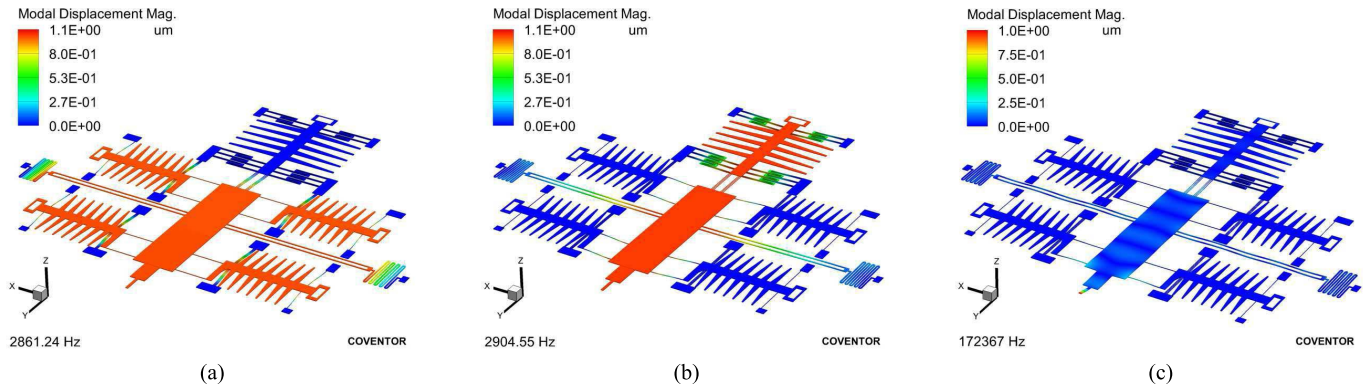
Fig. 2. Finite element model simulation of the mode shapes of the fundamental mode of the (a) x axis, (b) y axis, and (c) cantilever out-of-plane mode at 172 kHz.

At the center of the device is a stage with dimensions of $2315\,\mu m \times 650\,\mu m$, while a two-section microcantilever is fabricated at the upper edge of the stage. The in-plane displacement of the stage is obtained using a parallel kinematic mechanism. Along the device's x axis, electrostatic actuators are implemented on both sides of the stage, enabling it to have a bidirectional displacement range. An electrostatic actuator is also implemented on one side of the stage along the y axis, resulting in unidirectional displacement in this direction. As is visible in the close-up view in Fig. 1, the actuators are connected to the stage via shuttle beams and tethering beams in both directions. Two sets of electrostatic actuators are implemented along the x axis to obtain higher force while mitigating potential in-plane rotation of the stage.

As the y axis has a relatively large unidirectional displacement range, using standard clamped-clamped beams as mechanical flexures can lead to the stage possessing a nonlinear force-displacement behavior. In [12], folded beam flexures are proposed that provide in-plane stiffness with negligible nonlinearity compared to clamped-clamped beams. We have exploited this characteristic by designing the y-axis flexures in a similar manner. As the stage has a bidirectional displacement range along the x axis, clamped-clamped beams can be used in this direction as their stiffness can be considered to be linear within the displacement range of interest. In addition, these beams have a smaller form factor compared to the folded flexures, leading to a more compact structure in this direction. The incorporated mechanical suspension systems in both axes are designed to prevent the occurrence of snap-in within the electrostatic actuators by providing sufficient longitudinal stiffness throughout the entire range of displacement and actuation voltages [11].

The implemented microcantilever has two sections, with the wider section having dimensions of $380\,\mu m \times 240\,\mu m$ and the narrower part being $260\,\mu m \times 40\,\mu m$. In order to oscillate the cantilever and simultaneously measure its vibration amplitude, an AlN piezoelectric layer with a thickness of $0.5\,\mu m$ is deposited on the wider section of the microcantilever. The signal routing for the piezoelectric layer and the electrical ground connections to the stage is performed using long beams with dimensions of $2.3\,mm \times 25\,\mu m$ and $2.3\,mm \times 10\,\mu m$, respectively. The width of these beams are minimized while considering the restrictions imposed by

the microfabrication process. Serpentine structures are also implemented at the anchor points of these beams to reduce their in-plane stiffness along the y direction.

During the design, the finite element model (FEM) of the probe scanner is constructed in CoventorWare to investigate its mechanical characteristics. The results of the FEM modal analysis are presented in Fig. 2. The device is designed such that its first two in-plane resonant modes are along the x and y axis as shown in Fig. 2(a) and (b), respectively. A resonance frequency of about 2.9 kHz is predicted for both axes, matching well with the experimental results shown in Fig. 4. In Fig. 2(c), a high-frequency (172 kHz) mode shape of the device is shown, which, due its large displacement and negligible induced motion in the rest of the device, is designed to be suitable for tapping-mode AFM imaging (compare experimental results in Section III and Fig. 5).

Electrothermal sensors are implemented for both axes to measure the in-plane motion of the stage. As is shown in a close-up view in Fig. 1, the sensor comprises two heaters in proximity to a heat sink, which is implemented as a part of each shuttle beam [34]. As the heat sink moves parallel to the heaters, the rate of heat transfer between the heaters and the heat sink changes. This leads to opposing variations in their temperature, and as a result, changes in the electrical resistance of the heaters. A transimpedance circuit (shown in more detail in [14]) is used to translate the electrical resistance changes of the heaters to a varying output voltage.

B. AFM Tip

A sharp tip was added to the fabricated probe scanner using a focused ion beam (FIB) system (FEI Nova NanoLab 200), allowing the device to be used to image a sample via tapping-mode AFM. This method of AFM tip fabrication has been utilized in both commercial cantilever production and research applications, and is capable of producing high-resolution, high-aspect-ratio tips [35]. Using ion beam deposition of platinum, a stepped support structure with a total height of approximately $9\,\mu m$ was first constructed at the end of the probe scanner's cantilever. A thin platinum needle was then deposited at the top of the support structure using electron beam deposition, yielding a tip $1.5\,\mu m$ in length and with a diameter of approximately 40 nm. SEM images of the deposited probe tip are shown in Fig. 1.
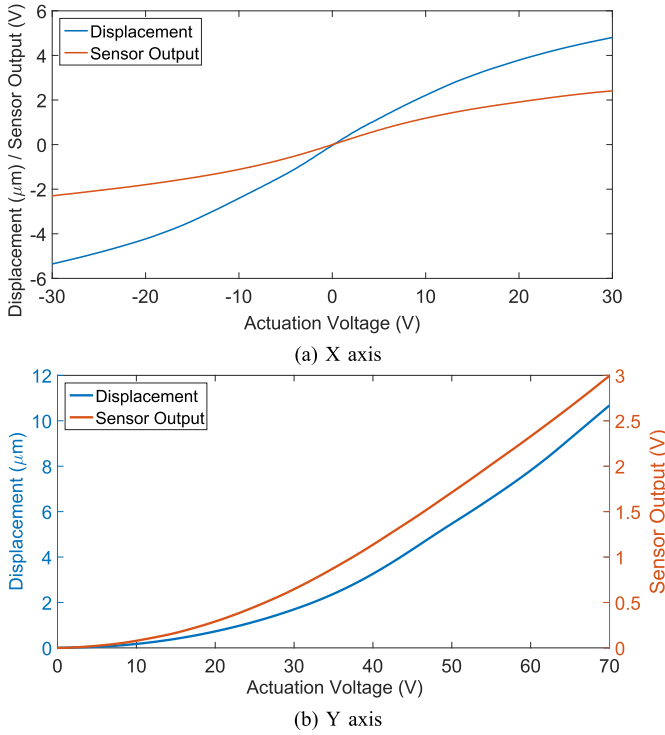
Fig. 3. In-plane displacement and corresponding electrothermal sensor output vs. actuation voltage for the probe scanner's x and y axes.

TABLE I
THE CALIBRATION FACTORS AND RESOLUTION OF THE
ELECTROTHERMAL SENSORS FOR X AND Y AXES

	x axis	y axis
Calibration factor $(\mathrm{V}/\mu\mathrm{m})$	0.468	0.285
1σ-Resolution (nm)	5.2	7.6

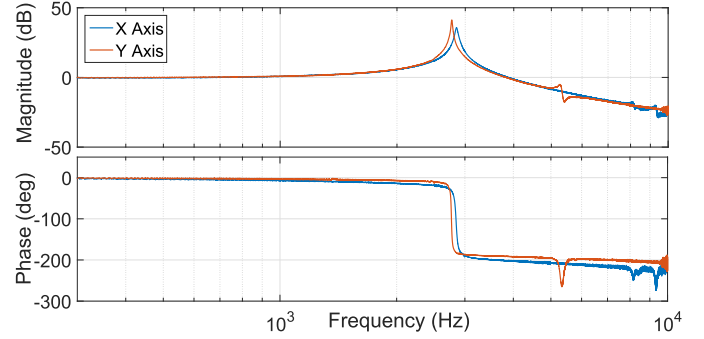

Fig. 4. The frequency response of the probe scanner along the x and y axes. For the sake of clarity, the DC gains are adjusted to unity.

While the use of an FIB system for tip fabrication is sufficient to demonstrate the operation of the probe scanner, a MEMS microfabricated tip is ultimately required to enable the cost-effective batch fabrication of the device. This is possible through techniques such as KOH wet etching or isotropic reactive ion etching [36], [37], which are currently being evaluated to enable the complete batch fabrication of future versions of the probe scanner.

III. XY-NANOPOSITIONER CHARACTERIZATION
AND CONTROL

The characterization of the fabricated system is performed while the electrothermal sensors are active with a 5 V bias voltage. As the electrostatic actuators along the x axis are implemented on both sides of the stage, a linear actuation mechanism can be implemented for this axis [14]. With this mechanism, the actuation signal is applied to the electrostatic actuators with opposite polarities while superimposed on a DC bias voltage, which is adjusted to be 35 V in our experiments. This mechanism can drastically alleviate the well-understood quadratic behavior of the electrostatic actuators [14].

The in-plane mechanism of the device is characterized in both the time and frequency domains. A low frequency triangular signal is applied to both axes, while their displacements are measured using a Polytec MSA-100-3D Micro System Analyzer (MSA). In Fig. 3, the in-plane displacement for both axes is shown as a function of the actuation signal. The displacement along the x axis slightly deviates from linear as shown in Fig. 3a. This can be attributed to nonlinearities in the stiffness of the clamped-clamped beams and possible asymmetry in the structure of the comb drive actuators.

The quadratic behavior of the y axis is also visible in Fig. 3b. A displacement range of more than $10\,\mu\mathrm{m}$ is obtained for both axes. The outputs of the electrothermal sensors are simultaneously recorded and are presented in the same figure for both axes. Each sensor's output is a linear function of the corresponding axis displacement, with the resulting calibration factors for the sensors being reported in Table I.

The frequency response of the in-plane mechanical structure is obtained for both axes using the MSA, and is shown in Fig. 4. As is visible, the first resonant modes along the x and y axes are located at 2.85 kHz and 2.77 kHz, respectively.

The out-of-plane vibration of the microcantilever is also characterized in the frequency domain by applying a wideband periodic chirp as an actuation signal to its piezoelectric transducer. During this test, the MSA is used to obtain the various out-of-plane mode shapes of the probe scanner by measuring the mechanical response of the device at a large number of points across its moving structure. The objective is to determine a mode shape within which the cantilever has a large enough oscillation amplitude to be used for tapping-mode AFM imaging while other parts of the device show negligible displacement. The experimental test shows that this criteria is best satisfied at the mode located at approximately 200 kHz, with Fig. 5 showing the vibration of the probe scanner at this mode.

To obtain the resolution of the electrothermal sensors, their output noise is characterized in the time-domain. The noise is recorded with a sampling frequency of 781 kHz over a time period of 12.8 s. A fourth-order anti-aliasing low-pass filter with a cut-off frequency of 100 kHz is employed by series connecting two Stanford Research SR560 low-noise voltage preamplifiers. The resolution of the sensors is reported in Table I, and is calculated by converting the root mean square (rms) value of the sensors' output noise to the corresponding displacement using their previously obtained calibration factors.
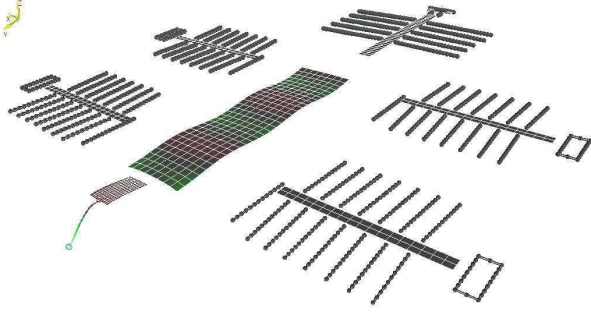
Fig. 5. The shape of the probe scanner's flexural mode used for AFM imaging, measured experimentally using the MSA.
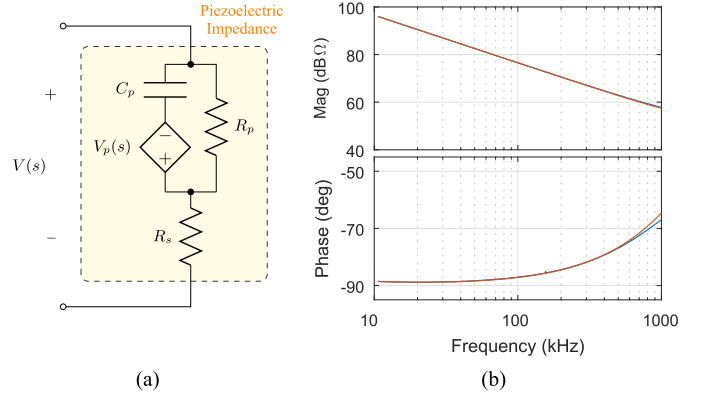

Fig. 6. (a) Electrical circuit model of the piezoelectric cantilever impedance with series parasitic resistance due to the silicon ground trace. (b) Frequency response of the complex impedance of the piezoelectric cantilever measured with an impedance analyzer (blue) and model (5) (red).

IV. CANTILEVER CHARACTERIZATION AND CONTROL

A. System Model

Assuming perfect bonding between the piezoelectric transducer and the cantilever beam and a clamped boundary condition at the base of the cantilever, a voltage applied to the electrodes results in a bending moment causing the cantilever to deflect. The transfer function from actuation voltage $V(s)$ to tip displacement $D(s)$ of the piezoelectric cantilever, can be described by a sum of n second order modes [38]

$$G_{dv}(s) = \frac{D(s)}{V(s)} = \sum_{i=1}^{n} \frac{\alpha_i \omega_i^2}{s^2 + \frac{\omega_i}{Q_i}s + \omega_i^2}, \quad (1)$$

where each second order term is associated with a specific vibrational mode shape and is characterized in terms of the respective resonance frequency ω_i, quality factor Q_i, and gain α_i. Similarly, when the piezoelectric transducer is subjected to mechanical strain, it becomes electrically polarized, producing a charge on the surface of the material. Neglecting parasitic effects, this direct piezoelectric effect can be modeled as a strain dependent voltage source $V_p(s)$ in series with the piezoelectric capacitance C_p, describing the dielectric properties of the material [30]. The model is a simplified version of the Butterworth Van Dyke model as proposed by the IEEE Standard on Piezoelectricity [39]. For this simplified case, the transfer function from actuation voltage to charge $Q(s)$ can be found to be [40]

$$G_{qv}(s) = \frac{Q(s)}{V(s)} = C_p + C_p \sum_{i=1}^{n} G_{vv,i}(s) \quad (2)$$

where

$$G_{vv}(s) = \frac{V_p(s)}{V(s)} = \sum_{i=1}^{n} \frac{\beta_i \omega_i^2}{s^2 + \frac{\omega_i}{Q_i}s + \omega_i^2} \quad (3)$$

is the transfer function from actuation voltage to piezoelectric strain voltage [41]. Observing that each mode in G_{dv} and G_{vv} only differ by a constant factor, (2) can be rewritten to yield

$$G_{qv}(s) = \frac{Q(s)}{V(s)} = C_p + C_p \sum_{i=1}^{n} \gamma_i G_{dv,i}(s). \quad (4)$$

From (4) it can be seen that a deflection estimate can be obtained by measuring the charge on the piezoelectric layer while the cantilever is being actively driven by a voltage source if the feedthrough $C_p V(s)$ can be canceled.

B. Piezoelectric Impedance

For this work, the above equivalent model is not sufficient to describe the electrical properties of the MEMS probe scanner. As such, it had to be amended by an additional parallel resistance R_p to take into account dielectric losses as well as a series resistance R_s which models the parasitic arising from the doped silicon ground trace. The equivalent electrical model of the piezoelectric layer is shown in the circuit diagram in Fig. 6(a). The resulting impedance $Z(s)$ can be calculated as

$$\begin{aligned} Z(s) &= R_p || C_p + R_s \\ &= \frac{R_s C_p R_p s + R_p + R_s}{C_p R_p s + 1}. \end{aligned} \quad (5)$$

To validate the model, the complex impedance ($|Z|$ in dBΩ, $\angle Z$ in deg) is measured with an impedance analyzer (Keysight, 4990A) and plotted in Fig. 6(b) and compared with the model (5). It can be seen that the extra zero caused by the series resistance R_s adequately describes the phase increase in the frequency range from 10 kHz to 1 MHz. The parallel resistance R_p creates a pole at low frequencies and does not contribute significantly to the behavior of $Z(s)$. Solving for the individual terms of the model (5) based on the identified model of the impedance transfer function shown in Fig. 6(b) yields the values shown in Table II.

C. Frequency Response

The frequency response of the piezoelectric cantilever from actuation voltage to tip deflection as measured with the optical beam deflection sensor of a commercial AFM (AFMWorkshop, TT-AFM) is shown in Fig. 7. Plotted alongside, is the identified transfer function model according to (1) capturing

TABLE II

IMPEDANCE MODEL PARAMETERS

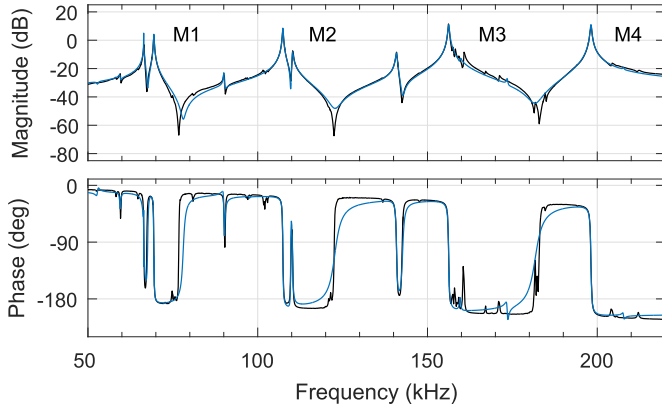| C_p (pF)	R_p (MΩ)	R_s (Ω)
237	3.12	318

Fig. 7. Frequency response of the probe scanner piezoelectric cantilever measured with the OBD sensor (black) and its identified model (1) (blue) highlighting the first four dominant flexural modes.

TABLE III
CANTILEVER MODEL PARAMETERS

Mode	f_i (kHz)	Q_i	k_i (N/m)
$M1$	69.4	403.4	484.3
$M2$	107.4	482.2	710.9
$M3$	156.0	564.7	928.4
$M4$	198.3	690.6	829.3

16 modes, including the four dominant out-of plane flexural modes as highlighted in the figure. The frequency response highlights the collocated nature of the eigenmodes of the probe scanner. Here, we chose the eigenmode M4 as the imaging mode for the reasons discussed in Section III.

D. Thermal Stiffness

A thermal noise spectrum was obtained by recording time-domain deflection data in free-air using the MSA sampled at 3.125 MHz for 8 s. From the measurement, the velocity power spectral density (PSD) estimate is calculated using Welch's method with 16 averages without overlap. The resulting PSD estimates for each of the four eigenmodes, highlighted in Fig. 7 are shown in Fig. 8 together with the Lorentzian function fits to determine the cantilever parameters resonance frequency f_i, quality (Q) factor Q_i, and modal stiffness k_i [42]–[44]. The identified parameters are summarized in Table III.

E. Piezoelectric Sensor Design

In order to measure the cantilever deflection using the piezoelectric transducer while simultaneously using the same layer for actuation, a self-sensing configuration is necessary. In previous works, the self-sensing interface with a piezoelectric cantilever was achieved using a low-side charge amplifier circuit situated at the opposite electrode of the piezoelectric layer with respect to the actuation signal [30]. While good results have been achieved with this configuration, in this work a different approach had to be taken due to the fact that the piezoelectric layer shares a common node with the rest of the electrical network of the MEMS device. In other words, the grounded electrode of the piezoelectric layer is not accessible. Therefore, an approach similar to the reciprocal self-sensing arrangement [32] had to be employed and is

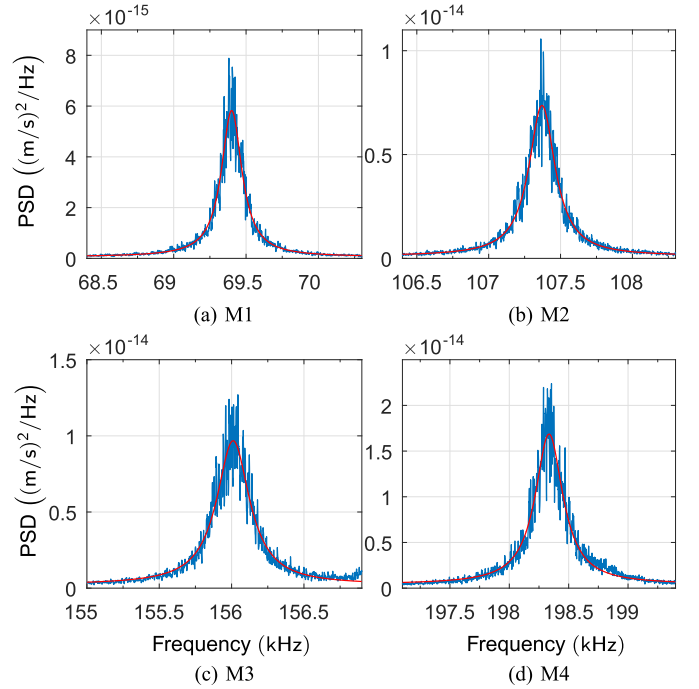(a) M1   (b) M2

(c) M3   (d) M4

Fig. 8. Velocity power spectral density estimate of Brownian motion (blue) obtained with a laser Doppler vibrometer and corresponding Lorentzian fit (red) of M1-M4 to determine modal resonance frequencies, Q-factors, and stiffnesses.
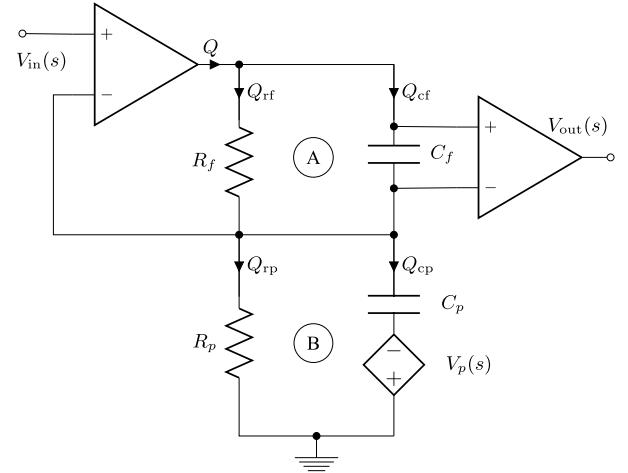

Fig. 9. Simplified circuit diagram of the piezoelectric high-side charge sensor.

subsequently termed high-side charge sensing. A simplified circuit diagram is shown in Fig. 9. Here, the driving op-amp maintains the input signal $V_{\text{in}}(s)$ across the piezoelectric layer and the charge generated by the strain dependent voltage source $V_p(s)$ is measured on a reference capacitor C_f on the same side as the actuation signal (therefore high-side charge sensor). To measure the charge on the reference capacitor, an instrumentation amplifier or a difference amplifier with a high-impedance buffer amplifier (on the node connected to the piezoelectric layer) should be employed. The transfer function of the sensor can be derived as follows (for the sake of simplicity the series resistance R_s is neglected in this analysis but will be taken into account for feedthrough cancellation in
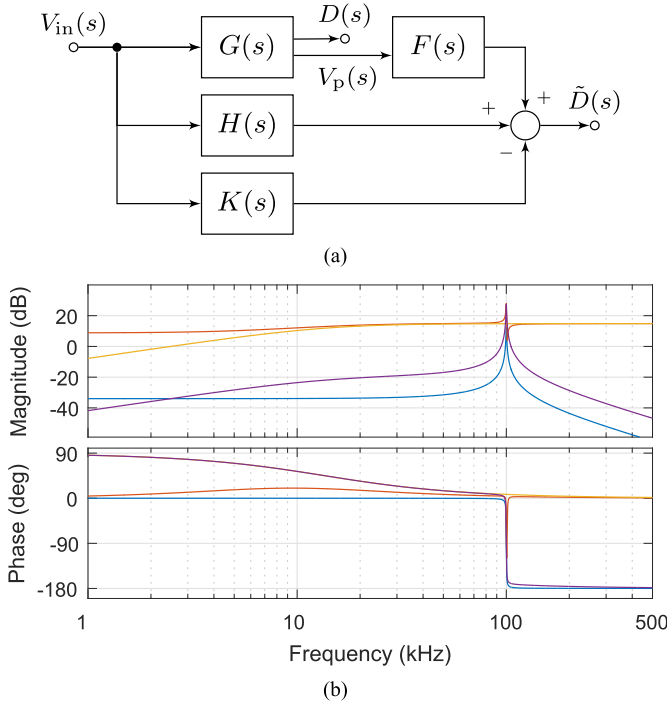
Fig. 10. (a) Block diagram showing the schematic setup of charge measurement and feedthrough cancellation. (b) Simulated single-mode transfer function $G_{dv}(s)$ (blue), sensor model (8) (red) and $F(s)$ (yellow) and recovered deflection estimate $F(s)V_p(s)$ (purple).
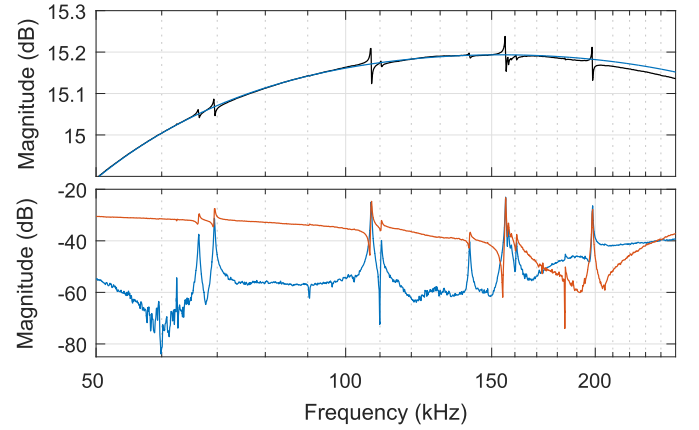

Fig. 11. Top: Frequency response of charge sensor (black) and fitted feedthrough compensator (second order bandpass filter) (blue). Bottom: Offline feedthrough cancellation using the exact model (blue) and an approximate model based on the realizable FPAA implementation (red).

the next subsection). The voltage across a resistor and across a capacitor can be written as a function of charge as $V_r = sQR$ and $V_c = Q/C$. Thus, we can write for loop A

$$Q(s) = \frac{C_f R_f s + 1}{C_f R_f s} Q_{cf}(s) \qquad (6)$$

and for loop B

$$Q(s) = \frac{C_p R_p s + 1}{R_p s} V_{in}(s) + C_p V_p(s). \qquad (7)$$

Equating (6) and (7) and solving for the voltage V_{cf} yields

$$\begin{aligned} V_{out}(s) &= \frac{R_f}{R_p} \frac{C_p R_p s + 1}{C_f R_f s + 1} V_{in}(s) + \frac{C_p R_f s}{C_f R_f s + 1} V_p(s) \\ &= H(s)V_{in}(s) + F(s)V_p(s). \end{aligned} \qquad (8)$$

It can be noticed that the transfer function (8) contains a feedthrough term $H(s)V_{in}(s)$ and that the motional term is filtered by a term $F(s)$. To develop a better understanding of the sensor behaviour, a simulation of the relevant transfer functions is shown in Fig. 10(b). It can be clearly observed how the feedthrough term heavily swallows the dynamics of the resonance. Moreover, it is noticeable that the feedthrough transfer function $H(s)$ and the motional filter $F(s)$ have the same pole which needs to be placed lower than the resonance frequency. This requirement dictates the choice of the sense impedance $R_f || C_f$ while keeping in mind that the high-frequency gain of the sensor is C_p/C_f and the low-frequency gain is R_f/R_p. At this point, a high piezo impedance $R_p || C_p$ is beneficial for the sensor design as it implies that the zero created by the piezo impedance is much smaller than the pole

due to the sense impedance. At the frequencies of interest, the resulting piezo impedance is quite low causing the zero to be placed at approximately 6.7 kHz. Therefore, the sense impedance is chosen to be $C_f = 47$ pF, $R_f = 250$ kΩ resulting in a pole at approximately 13.5 kHz.

In order to recover the motional signal from the sensor output, the feedthrough term $H(s)V_{in}(s)$ has to be canceled from the sensor signal in real-time. This can be done with a feedforward compensator $K(s)$ as schematically depicted in Fig. 10(a). Theoretically, the feedforward compensator is a first order lead lag element but due to the extra dynamics in the piezoelectric impedance associated with parasitic resistance in the MEMS device, a second order transfer function is estimated. The measured charge sensor frequency response is shown in Fig. 11. Clearly, the major resonances M1-M4 are visible, however unusable unless the feedthrough is removed. With the identified second order model of the feedthrough part, all the resonances can simultaneously be recovered offline as shown in Fig. 11. However, as the feedthrough cancellation is implemented on a Field Programmable Analog Array (FPAA) (Anadigm, AN221E04) additional constraints on the realizable second order filter limit the bandwidth in which the feedthrough can be accurately removed. Therefore, the filter has to be specifically tuned to a single mode which results in the simulated cancellation as shown in Fig. 11.

A second order biquadratic filter has been implemented on the FPAA based on the design discussed above. As can be seen in Fig. 12, around the mode of interest (M4 at $f \approx 200$ kHz), the mechanical resonance is recovered from the feedthrough resulting in a dynamic range of around 19 dB compared to a dynamic range of around 0.03 dB for the uncompensated frequency response (compare inset). In the vicinity of the resonance, the well matching phase and magnitude response with the frequency response taken with the OBD sensor indicates that the charge sensor output is purely related to the mechanical movement. Away from the resonance, it can be observed how the higher order nature of the feedthrough component results in a deviation from the mechanical frequency response.
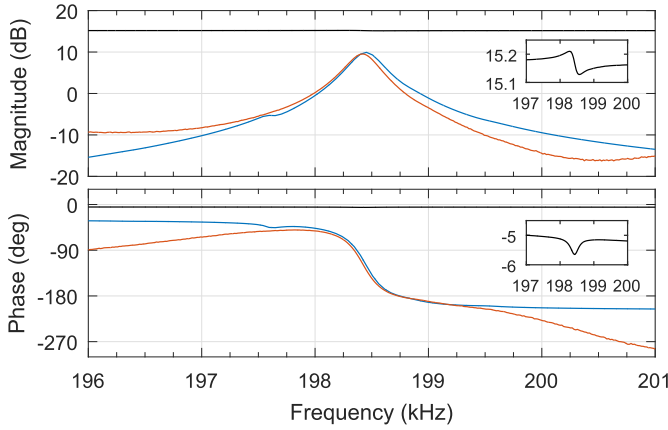
Fig. 12. Frequency response of the M4 mode of the probe scanner piezoelectric cantilever measured with the TT-AFM OBD sensor (blue), with the charge sensor before feedthrough cancellation (black) (the inset shows a zoomed view of the resonance) and after feedthrough cancellation (red). Magnitude and phase plots have been shifted such that the difference in dynamics is clearly visible.

V. TAPPING-MODE ATOMIC FORCE MICROSCOPY

A. Experimental Setup

To demonstrate on-chip tapping-mode atomic force microscopy, a commercial AFM (AFMWorkshop, TT-AFM) was employed to provide the sample approach functionality via the internal z axis stepper motor. The MEMS probe scanner was glued and wire bonded on to a printed circuit board (PCB) providing the piezoelectric sensing circuitry and signal routing for the xy actuators and sensor, and mounted on a custom-made 3D-printed probe holder. A larger PCB, containing the necessary circuitry for xy actuation and sensor signal conditioning, was placed further away and mounted on the TT-AFM. Photos of the setup are shown in Fig. 13. The piezoelectric self-sensing circuitry was driven by an external lock-in amplifier with integrated function generator (Zurich Instruments, HF2LI) which was also used to acquire the topography, magnitude, and phase images via a Matlab imaging script. The sample under investigation is a silicon NT-MDT TGZ3 calibration grating with periodic features of heights $h = 520 \pm 3$ nm. The lateral scan frequency was set to 1 Hz with a free-air amplitude of $A_0 \approx 130$ nm at an imaging setpoint of 60 %.

B. Tracking

To implement a raster scan trajectory for AFM imaging, a 1 Hz triangular signal is applied to the x axis while the y axis follows a slow ramp. An image size of 8 μm × 8 μm is chosen, and an integral controller with a gain of 120 is used for both axes to improve the tracking performance of the device. In Fig. 14, the tracking performance of the device along the x axis is shown. The rms value of the tracking error is 88 nm, however a significant component of this error is due to a time shift between the sensor output and reference, which does not affect the imaging quality. In addition, the imaging is only performed during the rising edge of the triangular signal. When considering only the rising edge of the reference signal and compensating for the time shift, the tracking error is about
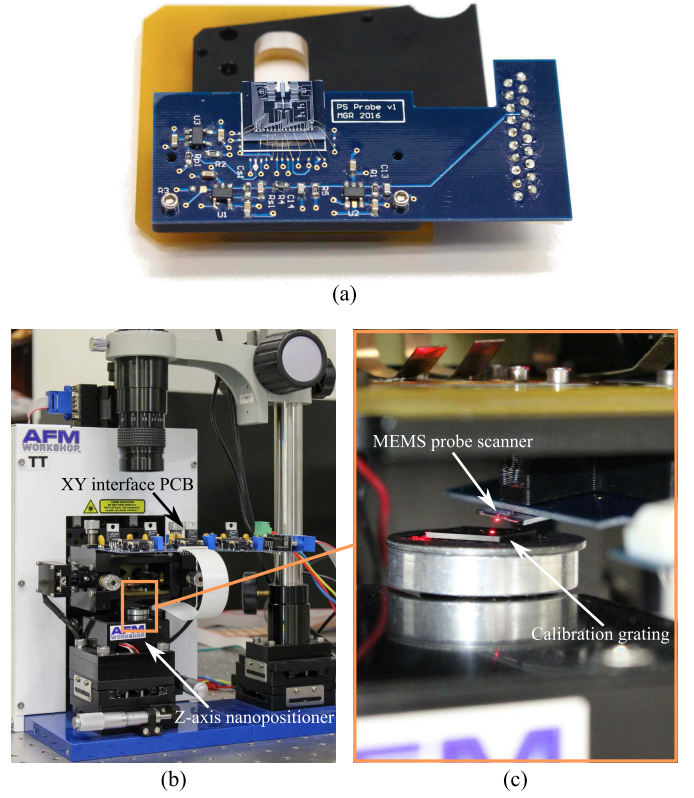

Fig. 13. Photos showing the experimental implementation of the MEMS probe scanner for AFM imaging. a) The MEMS probescanner die, fixed and wire bonded to the probe holder PCB. b) The probe scanner PCB installed in a commercial AFM, and connected via a flexible flat cable to an additional PCB containing the xy sensor readout circuits. c) A close-up view showing the MEMS probe scanner positioned above a calibration grating for AFM imaging (the OBD sensor is switched on to highlight the position of the cantilever).
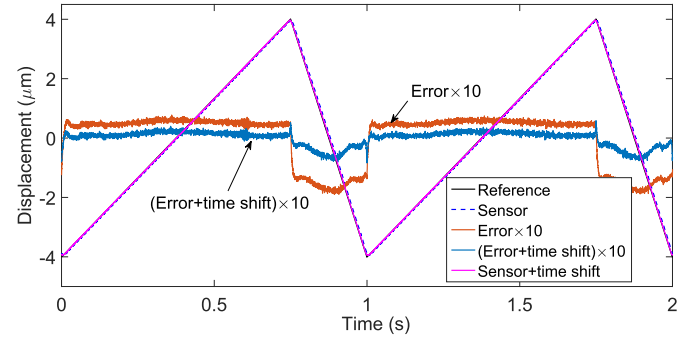

Fig. 14. Tracking performance of the stage along the x axis. The reference is a triangular signal with 4 μm peak-to-peak displacement. The error signals are compared before and after time delay compensation.

16 nm, which is approximately equal to the resolution of the sensor. The stage also satisfactorily tracks the slow ramp signal along the y axis with negligible error, which is not shown here for the sake of brevity.

C. AFM Imaging

A number of AFM images have been obtained, starting with a small scan range image of 4 μm × 4 μm with the xy actuators in open loop up to a scan range of 8 μm × 8 μm with integral control on the xy actuators to eliminate actuator nonlinearities. No image processing has been applied to the

(a) Topography 3D
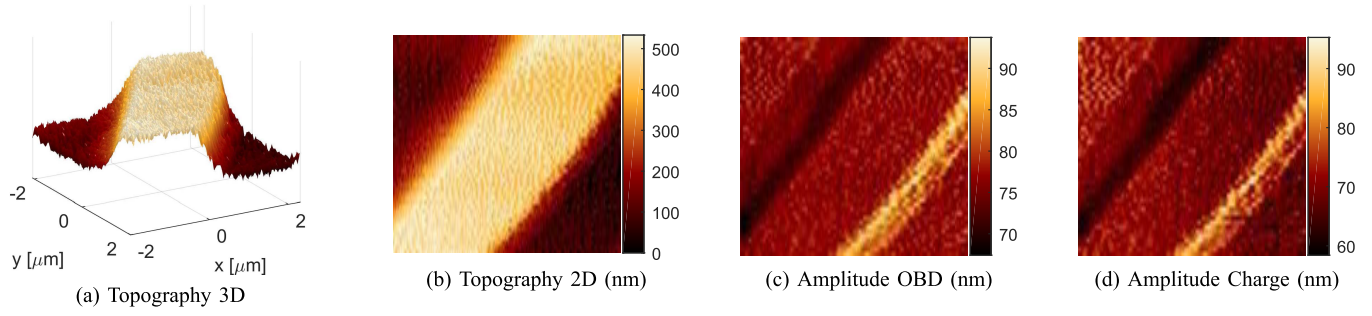
(b) Topography 2D (nm)

(c) Amplitude OBD (nm)

(d) Amplitude Charge (nm)

Fig. 15.   (a)-(d) 4 μm × 4 μm AFM image series with feedback from OBD sensor and parallel recording of the charge signal with the xy axes in open loop.

(a) Topography 3D
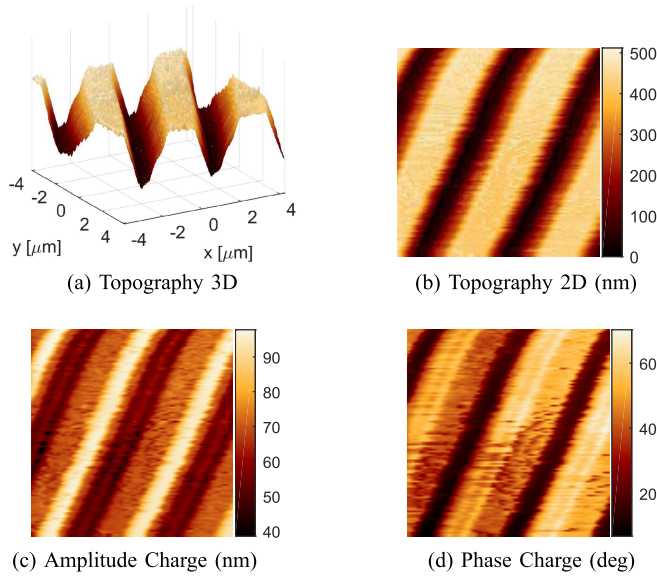
(b) Topography 2D (nm)

(c) Amplitude Charge (nm)

(d) Phase Charge (deg)

Fig. 16.   (a)-(d) 8 μm × 8 μm AFM image series with feedback from the charge sensor and xy axes in closed loop with integral controllers.

results; topography images have been plane corrected. Initially, the cantilever deflection was measured with the AFM-inherent OBD sensor and with the charge sensor in parallel, however ultimately the charge sensor was used to provide the feedback signal for topography imaging. It can be seen in the results shown in Fig. 15 that the OBD and charge sensor estimates show an equal amplitude error image, and that due to the open loop in the x and y directions some scanning nonlinearities are visible. These nonlinearities are largely eliminated by closing the loop in the x and y directions as can be seen in the results shown in Fig. 16 where the topography images are obtained with the charge sensor providing the z axis feedback signal. At the bottom of the features, it can be seen how the deteriorated state of the tip has led to a triangular artifact as compared to Fig. 15(a).

VI. CONCLUSION

We have presented an on-chip atomic force microscope for tapping-mode AFM imaging based on a silicon-on-insulator MEMS fabrication process. The device is equipped with electrostatic actuators that provide a maximum travel range of 10μm along the x and y directions. For these axes, electrothermal sensors are employed to control any tracking errors arising

from drift and nonlinearities with digitally implemented integral control. In the z direction, a single piezoelectric (AlN) actuator is used to actuate the cantilever at one of its resonance frequencies and a high-side charge sensor is used to recover the deflection signal from the piezoelectric signal. This is possible with a model-based feedthrough cancellation scheme implemented on an FPAA. The device was equipped with a post-fabricated FIB tip and thereafter successfully used to image a calibration grating. Future work will focus on improving the piezoelectric impedance properties over frequency and possibly separate actuation and sensing such that feedthrough cancellation can be avoided. The authors are currently working on a revised design incorporating the tip fabrication step into the device fabrication.

REFERENCES

[1] G. Binnig, C. F. Quate, and C. Gerber, "Atomic force microscope," *Phys. Rev. Lett.*, vol. 56, pp. 930–933, Mar. 1986.

[2] Y. K. Yong, S. O. R. Moheimani, B. J. Kenton, and K. K. Leang, "Invited review article: High-speed flexure-guided nanopositioning: Mechanical design and control issues," *Rev. Sci. Instrum.*, vol. 83, no. 12, p. 121101, 2012.

[3] M. W. Fairbairn and S. O. R. Moheimani, "Control techniques for increasing the scan speed and minimizing image artifacts in tapping-mode atomic force microscopy: Toward video-rate nanoscale imaging," *IEEE Control Syst.*, vol. 33, no. 6, pp. 46–67, Dec. 2013.

[4] L. L. Chu and Y. B. Gianchandani, "A micromachined 2D positioner with electrothermal actuation and sub-nanometer capacitive sensing," *J. Micromech. Microeng.*, vol. 13, no. 2, pp. 279–285, 2003.

[5] X. Liu, K. Kim, and Y. Sun, "A MEMS stage for 3-axis nanopositioning," *J. Micromech. Microeng.*, vol. 17, no. 9, pp. 1796–1802, Sep. 2007.

[6] D. M. Brouwer, B. R. De Jong, and H. M. J. R. Soemers, "Design and modeling of a six DOFs MEMS-based precision manipulator," *Precis. Eng.*, vol. 34, no. 2, pp. 307–319, Apr. 2010.

[7] S. Bergna, J. J. Gorman, and N. G. Dagalakis, "Design and modeling of thermally actuated MEMS nanopositioners," in *Proc. ASME Int. Mech. Eng. Congr. Expo.*, Orlando, FL, USA, Nov. 2005, pp. 1–8.

[8] Y. Zhu, A. Bazaei, S. O. R. Moheimani, and M. R. Yuce, "Design, modeling, and control of a micromachined nanopositioner with integrated electrothermal actuation and sensing," *J. Microelectromech. Syst.*, vol. 20, no. 3, pp. 711–719, 2011.

[9] A. G. Fowler, A. N. Laskovski, A. C. Hammond, and S. O. R. Moheimani, "A 2-DOF electrostatically actuated MEMS nanopositioner for on-chip AFM," *J. Microelectromech. Syst.*, vol. 21, no. 4, pp. 771–773, 2012.

[10] M. Maroufi, A. G. Fowler, A. Bazaei, and S. O. Reza Moheimani, "High-stroke silicon-on-insulator MEMS nanopositioner: Control design for non-raster scan atomic force microscopy," *Rev. Sci. Instrum.*, vol. 86, no. 2, pp. 023705-1–023705-12, 2015.

[11] M. Maroufi, A. G. Fowler, and S. O. R. Moheimani, "MEMS nanopositioner for on-chip atomic force microscopy: A serial kinematic design," *J. Microelectromech. Syst.*, vol. 24, no. 6, pp. 1730–1740, 2015.

[12] M. Maroufi and S. O. R. Moheimani, "A 2DOF SOI-MEMS nanopositioner with tilted flexure bulk piezoresistive displacement sensors," *IEEE Sensors J.*, vol. 16, no. 7, pp. 1908–1917, Apr. 2016.

[13] A. Mohammadi, A. G. Fowler, Y. K. Yong, and S. O. R. Moheimani, "A feedback controlled MEMS nanopositioner for on-chip high-speed AFM," *J. Microelectromech. Syst.*, vol. 23, no. 3, pp. 610–619, 2014.

[14] M. Maroufi, A. Bazaei, and S. O. R. Moheimani, "A high-bandwidth MEMS nanopositioner for on-chip AFM: Design, characterization, and control," *IEEE Trans. Control Syst. Technol.*, vol. 23, no. 2, pp. 504–512, Mar. 2015.

[15] A. Bazaei, M. Maroufi, A. G. Fowler, and S. O. R. Moheimani, "Internal model control for spiral trajectory tracking with MEMS AFM scanners," *IEEE Trans. Control Syst. Technol.*, vol. 24, no. 5, pp. 1717–1728, Sep. 2016.

[16] N. Sarkar, R. R. Mansour, O. Patange, and K. Trainor, "CMOS-MEMS atomic force microscope," in *Proc. 16th Int. Solid-State Sens. Actuators Microsyst. Conf. (TRANSDUCERS)*, Beijing, China, Jun. 2011, pp. 2610–2613.

[17] N. Sarkar, G. Lee, D. Strathearn, M. Olfat, and R. R. Mansour, "A multimode single-chip scanning probe microscope for simultaneous topographical and thermal metrology at the nanometer scale," in *Proc. IEEE 29th Int. Conf. Micro Electro Mech. Syst. (MEMS)*, Shanghai, China, Jan. 2016, pp. 55–58.

[18] D. J. Bell, T. J. Lu, N. A. Fleck, and S. M. Spearing, "MEMS actuators and sensors: Observations on their performance and selection for purpose," *J. Micromech. Microeng.*, vol. 15, no. 7, pp. S153–S164, Jun. 2005.

[19] N. B. Hubbard, M. L. Culpepper, and L. L. Howell, "Actuators for micropositioners and nanopositioners," *Appl. Mech. Rev.*, vol. 59, no. 6, pp. 324–334, 2006.

[20] L. Que, J.-S. Park, and Y. B. Gianchandani, "Bent-beam electrothermal actuators—Part I: Single beam and cascaded devices," *J. Microelectromech. Syst.*, vol. 10, no. 2, pp. 247–254, Jun. 2001.

[21] G. Meyer and N. M. Amer, "Novel optical approach to atomic force microscopy," *Appl. Phys. Lett.*, vol. 53, no. 12, pp. 1045–1047, 1988.

[22] W. Han, S. M. Lindsay, and T. Jing, "A magnetically driven oscillating probe microscope for operation in liquids," *Appl. Phys. Lett.*, vol. 69, no. 26, pp. 4111–4113, 1996.

[23] N. Umeda, S. Ishizaki, and H. Uwai, "Scanning attractive force microscope using photothermal vibration," *J. Vac. Sci. Technol. B*, vol. 9, no. 2, pp. 1318–1322, 1991.

[24] K. Yamanaka and S. Nakano, "Ultrasonic atomic force microscope with overtone excitation of cantilever," *Jpn. J. Appl. Phys.*, vol. 35, no. 6B, pp. 3787–3792, 1996.

[25] G. E. Fantner *et al.*, "Use of self-actuating and self-sensing cantilevers for imaging biological samples in fluid," *Nanotechnology*, vol. 20, no. 43, p. 434003, 2009.

[26] P.-F. Indermühle, G. Schürmann, G.-A. Racine, and N. De Rooij, "Fabrication and characterization of cantilevers with integrated sharp tips and piezoelectric elements for actuation and detection for parallel AFM applications," *Sens. Actuators A, Phys.*, vol. 60, nos. 1–3, pp. 186–190, 1997.

[27] T. Göddenhenrich, H. Lemke, U. Hartmann, and C. Heiden, "Force microscope with capacitive displacement detection," *J. Vac. Sci. Technol. A*, vol. 8, no. 1, pp. 383–387, 1990.

[28] M. Tortonese, R. C. Barrett, and C. F. Quate, "Atomic resolution with an atomic force microscope using piezoresistive detection," *Appl. Phys. Lett.*, vol. 62, no. 8, pp. 834–836, 1993.

[29] T. Itoh and T. Suga, "Development of a force sensor for atomic force microscopy using piezoelectric thin films," *Nanotechnology*, vol. 4, no. 4, p. 218, 1993.

[30] M. G. Ruppert and S. O. R. Moheimani, "A novel self-sensing technique for tapping-mode atomic force microscopy," *Rev. Sci. Instrum.*, vol. 84, no. 12, p. 125006, 2013.

[31] A. G. Fowler, M. Maroufi, and S. O. R. Moheimani, "A silicon-on-insulator microelectromechanical systems probe scanner for on-chip atomic force microscopy," *Rev. Sci. Instrum.*, vol. 86, no. 4, p. 046107, 2015.

[32] M. G. Ruppert and S. O. R. Moheimani, "Novel reciprocal self-sensing techniques for tapping-mode atomic force microscopy," in *Proc. 19th IFAC World Congr.*, Cape Town, South Africa, Aug. 2014, pp. 7474–7479.

[33] A. Cowen, G. Hames, K. Glukh, and B. Hardy, *PiezoMUMPs Design Handbook*, 1st ed. Durham, NC, USA: MEMSCAP Inc., 2014.

[34] B. Krijnen *et al.*, "A single-mask thermal displacement sensor in MEMS," *J. Micromech. Microeng.*, vol. 21, no. 7, p. 074007, 2011.

[35] I. Utke, P. Hoffmann, and J. Melngailis, "Gas-assisted focused electron beam and ion beam processing and fabrication," *J. Vac. Sci. Technol. B, Microelectron. Nanometer Struct.*, vol. 26, no. 4, p. 1197, 2008.

[36] M. A. R. Alves, D. F. Takeuti, and E. S. Braga, "Fabrication of sharp silicon tips employing anisotropic wet etching and reactive ion etching," *Microelectron. J.*, vol. 36, no. 1, pp. 51–54, Jan. 2005.

[37] L. Yifang, W. Lingyun, and S. Daoheng, "Fabrication of nano-tips employing three different methods," in *Proc. Int. Technol. Innovation Conf.*, Hangzhou, China, 2006, pp. 1298–1301.

[38] M. G. Ruppert and S. O. R. Moheimani, "Multimode Q control in tapping-mode AFM: Enabling imaging on higher flexural eigenmodes," *IEEE Trans. Control Syst. Technol.*, vol. 24, no. 4, pp. 1149–1159, Jul. 2016.

[39] A. H. Meitzler, H. F. Tiersten, A. W. Warner, D. Berlincourt, and G. A. Coquin, *IEEE Standard on Piezoelectricity*, ANSI/IEEE Standard 176–1987, 1988.

[40] M. G. Ruppert and S. O. R. Moheimani, "High-bandwidth multimode self-sensing in bimodal atomic force microscopy," *Beilstein J. Nanotechnol.*, vol. 7, pp. 284–295, Oct. 2016.

[41] S. O. R. Moheimani and A. J. Fleming, *Piezoelectric Transducers for Vibration Control and Damping*. London, U.K.: Springer-Verlag, 2006.

[42] H.-J. Butt and M. Jaschke, "Calculation of thermal noise in atomic force microscopy," *Nanotechnology*, vol. 6, no. 1, p. 1, 1995.

[43] J. R. Lozano, D. Kiracofe, J. Melcher, R. Garcia, and A. Raman, "Calibration of higher eigenmode spring constants of atomic force microscope cantilevers," *Nanotechnology*, vol. 21, no. 46, p. 465502, 2010.

[44] J. E. Sader *et al.*, "Spring constant calibration of atomic force microscope cantilevers of arbitrary shape," *Rev. Sci. Instrum.*, vol. 83, no. 10, p. 103705, 2012.

Michael G. Ruppert (S'14) received the Dipl.-Ing. degree in automation technology in production, with a specialization in systems theory and automatic control, from the University of Stuttgart, Stuttgart, Germany, in 2013. He is currently pursuing the Ph.D. degree in electrical engineering from The University of Newcastle, Callaghan, NSW, Australia. As a Visiting Researcher, he was with the Mechanical Engineering Department, University of Texas at Dallas, USA. His current research interests include the utilization of system theoretic tools for sensing, estimation, and control in multifrequency atomic force microscopy.

Mr. Ruppert received the Academic Merit Scholarship from the University of Stuttgart, the Baden-Württemberg Scholarship, and holds Postgraduate Research Scholarships with the University of Newcastle and with the CSIRO, Clayton, VIC, Australia.

Anthony G. Fowler (S'10–M'15) received the bachelor's and Ph.D. degrees in electrical engineering from The University of Newcastle, Callaghan, NSW, Australia, in 2010 and 2014, respectively.

From 2014 to 2015 he was a Post-Doctoral Fellow with the School of Electrical Engineering and Computer Science, The University of Newcastle. He is currently a Research Scientist with the Department of Mechanical Engineering, University of Texas at Dallas, Richardson, TX, USA. His current research interests include the design, fabrication, and analysis of novel microelectromechanical systems for energy harvesting, nanopositioning, and scanning probe microscopy applications.

Mohammad Maroufi (M'16) received the B.Sc. degrees in mechanical engineering and applied physics, as a distinguished student, the master's degree in mechatronics from the Amirkabir University of Technology in 2008 and 2011, respectively, and the Ph.D. degree in electrical engineering from The University of Newcastle, Australia, in 2015. He is currently a Research Associate with the Department of Mechanical Engineering, University of Texas at Dallas. His research interests include the design and control of MEMS nanopositioning systems, MEMS based sensing and actuation, on-chip atomic force microscopy, and modeling of smart materials and structures.

S. O. Reza Moheimani (F'11) currently holds the James Von Ehr Distinguished Chair in science and technology with the Department of Mechanical Engineering, University of Texas at Dallas. His current research interests include ultrahigh-precision mechatronic systems, with particular emphasis on dynamics and control at the nanometer scale, including applications of control and estimation in nanopositioning systems for high-speed scanning probe microscopy and nanomanufacturing, modeling and control of microcantilever-based devices, control of microactuators in microelectromechanical systems, and design, modeling, and control of micromachined nanopositioners for on-chip scanning probe microscopy.

Dr. Moheimani is a fellow of the IFAC and the Institute of Physics, U.K. His research has been recognized with a number of awards, including the IFAC Nathaniel B. Nichols Medal in 2014, the IFAC Mechatronic Systems Award in 2013, the IEEE Control Systems Technology Award in 2009, the IEEE Transactions on Control Systems Technology Outstanding Paper Award in 2007, and several best paper awards in various conferences. He is the Editor-in-Chief of Mechatronics and has served on the editorial boards of a number of other journals, including the IEEE TRANSACTIONS ON MECHATRONICS, the IEEE TRANSACTIONS ON CONTROL SYSTEMS TECHNOLOGY, and the *Control Engineering Practice*. He is currently the Chair of the IFAC Technical Committee on Mechatronic Systems.